



The New Magnetar SGR J1830–0645 in Outburst

F. Coti Zelati^{1,2}, A. Borghese^{1,2}, G. L. Israel³, N. Rea^{1,2}, P. Esposito^{4,5}, M. Pilia⁶, M. Burgay⁶, A. Possenti^{6,7},
A. Corongiu⁶, A. Ridolfi^{6,8}, C. Dehman^{1,2}, D. Viganò^{1,2}, R. Turolla^{9,10}, S. Zane¹⁰, A. Tiengo^{4,5,11}, and
E. F. Keane^{12,13}

¹ Institute of Space Sciences (ICE, CSIC), Campus UAB, Carrer de Can Magrans s/n, E-08193, Barcelona, Spain; cotizelati@ice.csic.es

² Institut d'Estudis Espacials de Catalunya (IEEC), Carrer Gran Capità 2–4, E-08034 Barcelona, Spain

³ INAF—Osservatorio Astronomico di Roma, via Frascati 33, I-00078 Monteporzio Catone, Italy

⁴ Scuola Universitaria Superiore IUSS Pavia, Palazzo del Broletto, piazza della Vittoria 15, I-27100 Pavia, Italy

⁵ INAF—Istituto di Astrofisica Spaziale e Fisica Cosmica di Milano, via A. Corti 12, I-20133 Milano, Italy

⁶ INAF—Osservatorio Astronomico di Cagliari, Via della Scienza 5, I-09047 Selargius, Italy

⁷ Department of Physics, Università di Cagliari, S.P. Monserrato-Sestu km 0,700, I-09042 Monserrato, Italy

⁸ Max Planck Institute für Radioastronomie, Auf dem Hügel 69, D-53121 Bonn, Germany

⁹ Dipartimento di Fisica e Astronomia “Galileo Galilei,” Università di Padova, via F. Marzolo 8, I-35131 Padova, Italy

¹⁰ Mullard Space Science Laboratory, University College London, Holmbury St. Mary, Dorking, Surrey RH5 6NT, UK

¹¹ Istituto Nazionale di Fisica Nucleare (INFN), Sezione di Pavia, via A. Bassi 6, I-27100 Pavia, Italy

¹² SKA Organisation, Jodrell Bank, Macclesfield, Cheshire, SK11 9FT, UK

¹³ Centre for Astronomy, School of Physics, National University of Ireland Galway, University Road, Galway, H91 TK33, Ireland

Received 2020 November 17; revised 2020 December 22; accepted 2021 January 11; published 2021 January 29

Abstract

The detection of a short hard X-ray burst and an associated bright soft X-ray source by the Swift satellite in 2020 October heralded a new magnetar in outburst, SGR J1830–0645. Pulsations at a period of ~ 10.4 s were detected in prompt follow-up X-ray observations. We present here the analysis of the Swift/Burst Alert Telescope burst, of XMM-Newton and the Nuclear Spectroscopic Telescope Array observations performed at the outburst peak, and of a Swift/X-ray Telescope monitoring campaign over the subsequent month. The burst was single-peaked, lasted ~ 6 ms, and released a fluence of $\approx 5 \times 10^{-9}$ erg cm $^{-2}$ (15–50 keV). The spectrum of the X-ray source at the outburst peak was well described by an absorbed double-blackbody model plus a power-law component detectable up to ~ 25 keV. The unabsorbed X-ray flux decreased from $\sim 5 \times 10^{-11}$ to $\sim 2.5 \times 10^{-11}$ erg cm $^{-2}$ s $^{-1}$ one month later (0.3–10 keV). Based on our timing analysis, we estimate a dipolar magnetic field $\approx 5.5 \times 10^{14}$ G at pole, a spin-down luminosity $\approx 2.4 \times 10^{32}$ erg s $^{-1}$, and a characteristic age ≈ 24 kyr. The spin modulation pattern appears highly pulsed in the soft X-ray band, and becomes smoother at higher energies. Several short X-ray bursts were detected during our campaign. No evidence for periodic or single-pulse emission was found at radio frequencies in observations performed with the Sardinia Radio Telescope and Parkes. According to magneto-thermal evolutionary models, the real age of SGR J1830–0645 is close to the characteristic age, and the dipolar magnetic field at birth was slightly larger, $\sim 10^{15}$ G.

Unified Astronomy Thesaurus concepts: Magnetars (992); Pulsars (1306); X-ray transient sources (1852); X-ray bursts (1814); Magnetic fields (994); X-ray point sources (1270)

1. Introduction

The term “magnetar” was coined almost three decades ago to identify isolated neutron stars (NSs) ultimately powered by the dissipation of their own magnetic energy, which usually implies that they are endowed with huge magnetic fields, up to $\sim 10^{15}$ G (Duncan & Thompson 1992). A large fraction of the ~ 30 magnetars known to date (Olausen & Kaspi 2014) have been discovered just over the past two decades, through their distinctive high-energy phenomenology: bursts of X-ray/gamma-ray emission and/or enhancements of their persistent X-ray luminosity, dubbed “outbursts” (see Kaspi & Beloborodov 2017; Esposito et al. 2021). The bursts are comparatively brief episodes lasting from milliseconds to hundreds of seconds, and reaching X-ray peak luminosities within the interval 10^{39} – 10^{47} erg s $^{-1}$ (e.g., Collazzi et al. 2015). The outbursts are instead long-lasting events where the X-ray luminosity first rises to values in the range of 10^{34} – 10^{36} erg s $^{-1}$, and then decreases on timescales that can be as long as years (Coti Zelati et al. 2018). Remarkably, in a couple of magnetars the post-outburst luminosity was found to differ from the pre-outburst long-term persistent level (Younes et al. 2017; Coti Zelati et al. 2020).

On 2020 October 10 at 14:49:24 UT, the Burst Alert Telescope (BAT) on board the Neil Gehrels Swift Observatory triggered on a short, hard X-ray burst (Page et al. 2020). Prompt observations with the Swift X-ray Telescope (XRT) localized a new uncatalogued X-ray source, SGR J1830–0645.¹⁴ An X-ray periodic signal at ~ 10.4 s was detected in the XRT data (Gogus et al. 2020a) and confirmed later by observations with the Neutron Star Interior Composition Explorer (NICER) (Younes et al. 2020). The burst properties, the periodicity detected in the prompt follow-up observations, and the proximity of the source to the Galactic plane (Galactic latitude $b \sim 1^\circ 5$) point to a newly discovered magnetar in outburst.

This Letter reports on (i) the properties of the X-ray bursts detected from SGR J1830–0645 by the Swift/BAT; (ii) quasi-simultaneous observations with XMM-Newton and the Nuclear Spectroscopic Telescope Array (NuSTAR) performed within ~ 2 days after the first BAT burst; (iii) a Swift/XRT monitoring campaign covering the first month since the outburst onset;

¹⁴ Tohuvavohu (2020) reported the discovery in an offline search of the BAT data of another burst from SGR J1830–0645 which, however, did not result in a detector trigger.

(iv) a search for short bursts in the X-ray time series (Section 2); and (v) radio observations with the Sardinia Radio Telescope and Parkes (Section 3). Discussion and conclusions follow (Section 4).

2. X-Ray Emission

2.1. Observations and Data Analysis

Table 1 reports a log of the X-ray observations. Data reduction was performed using tools incorporated in HEASOFT (v.6.28) and the Science Analysis Software (v.19) with the latest calibration files. Photon arrival times were barycentered using the Chandra position (Gogus et al. 2020b), R.A. = $18^{\text{h}}30^{\text{m}}41^{\text{s}}.64$, decl. = $-06^{\circ}45'16''.9$ (J2000.0; uncertainty of $0''.8$ at 90% c.l.¹⁵) and the JPL planetary ephemeris DE-405. The spectral analysis was performed using the XSPEC package (Arnaud 1996), adopting the TBABS model (Wilms et al. 2000) to describe the interstellar absorption. Hereafter, all uncertainties are quoted at 1σ c.l.

2.1.1. Swift

For the burst that revealed SGR J1830–0645 by alerting the BAT and two other events detected on 2020 November 5 and 11, we extracted mask-tagged light curves and spectra using standard tools in the FTOOLS software package. SGR J1830–0645 was observed 14 times with the XRT (Burrows et al. 2005) configured either in photon counting (PC; timing resolution of 2.5 s), or windowed timing (WT; 1.8 ms) mode. The source photons were extracted from a circular region of radius 20 pixels (1 pixel = $2''.36$). Background events were collected from a circle of the same size for WT-mode data and an annulus with radii 40–80 pixels for PC-mode data. In the first pointing (obs.ID 00999571000), photons within the inner 4 pixels of the source point-spread function were removed to minimize pile-up effects.

2.1.2. XMM-Newton

SGR J1830–0645 was observed with the European Photon Imaging Cameras (EPIC) on board XMM-Newton on 2020 October 11–12, for an exposure time of 23.6 ks. The EPIC-pn (Strüder et al. 2001) and the MOS (Turner et al. 2001) cameras were operating in Small Window mode (SW; timing resolutions of 5.7 ms and 0.3 s, respectively). Here, we consider only the data acquired with the EPIC-pn, which provides the data set with the highest counting statistics owing to its larger effective area compared to the MOS cameras.

Raw data were processed following standard analysis procedures. No periods of high background activity were detected. The source events were selected from a circle with a radius of $40''$ and the background counts were accumulated from a closely by circle of the same size. The response matrices and ancillary files were generated through the RMFGEN and ARFGEN tools, respectively. Background-subtracted and exposure-corrected light curves were extracted using the EPICL-CORR task.

2.1.3. NuSTAR

NuSTAR (Harrison et al. 2013) observed SGR J1830–0645 on 2020 October 12 for an effective exposure time of 29.6 ks.

We created cleaned event files and filtered out passages through the South Atlantic Anomaly using the tool NUPIPELINE with default options. For both focal plane modules (FPMA and FPMB), we collected the source counts within a circle of radius $100''$ and estimated the background from four circles of the same size located on all detectors using the NUSKYBGD pipeline (Wik et al. 2014). The source was detected up to an energy of ~ 25 keV in both FPMs. We ran the tool NUPRODUCTS to extract light curves and spectra, and to generate response files.

2.2. Results

2.2.1. BAT Bursts Properties

Figure 1 shows the time evolution of the burst detected on 2020 October 10 in the 15–50 keV band (no emission is detected at higher energies). The event was single-peaked and had a total duration and a T_{90} duration,¹⁶ as computed from a Bayesian blocks analysis with the BATTBLOCKS tool, of 6 ± 1 ms and 5 ± 1 ms, respectively. The spectrum extracted from the whole interval, similarly to standard magnetar bursts seen at hard X-rays, can be described in the 15–50 keV band by simple models, such as a blackbody with temperature $kT = 8.0_{-1.2}^{+1.6}$ keV (with reduced χ^2 of $\chi_r^2 = 1.05$ for 14 degrees of freedom (d.o.f.)) or a power law with photon index $\Gamma = 1.9 \pm 0.5$ ($\chi_r^2 = 1.12$ for 14 d.o.f.). For the blackbody model, the average flux was $7.6_{-3.3}^{+0.4} \times 10^{-7}$ erg cm⁻² s⁻¹, corresponding to a fluence of $\sim 4.6 \times 10^{-9}$ erg cm⁻² (15–50 keV). Two other bursts resulted in BAT triggers during our campaign (see Palmer 2020). The second burst detected on 2020 November 5 was longer (25 ± 5 ms, $T_{90} = 21 \pm 5$ ms) and harder, being visible in the light curve up to ≈ 150 keV. Also in this case, the adoption of a blackbody model resulted in the best fit, with $\chi_r^2 = 0.83$ for 56 d.o.f., and $kT = 9.8 \pm 0.7$ keV. The average flux was $(1.3 \pm 0.1) \times 10^{-6}$ erg cm⁻² s⁻¹, while the fluence was $\sim 3.2 \times 10^{-8}$ erg cm⁻² (15–150 keV). The burst that triggered BAT on 2020 November 11 was intermediate in hardness between the other two events, and lasted 26 ± 6 ms ($T_{90} = 21 \pm 7$ ms). For the blackbody model ($kT = 9.1 \pm 0.6$ keV; $\chi_r^2 = 0.67$ for 56 d.o.f.), the average flux was $(8.1 \pm 0.7) \times 10^{-7}$ erg cm⁻² s⁻¹ and the fluence $\sim 2.2 \times 10^{-8}$ erg cm⁻² (15–150 keV).

2.2.2. X-Ray Monitoring and Archival Observations

First, we fit the broadband spectrum extracted from the quasi-simultaneous EPIC-pn and NuSTAR data sets using models comprising different combinations of blackbody and power-law components. We included a constant term in the fits to account for inter-calibration uncertainties between the three instruments, deriving a mismatch of $<5\%$ for all the tested models. The best description of the data was provided by an absorbed double-blackbody model plus a power-law component accounting for emission at energies above ~ 12 keV (Figure 1), giving $\chi_r^2 = 1.10$ for 376 d.o.f. and a null hypothesis probability $\text{nhp} \simeq 0.10$. Best-fitting parameters were absorption column density $N_{\text{H}} = (1.07 \pm 0.02) \times 10^{22}$ cm⁻², blackbody temperatures and radii $kT_{\text{BB,W}} = 0.45 \pm 0.01$ keV, $R_{\text{BB,W}} = 5.6 \pm 0.3$ km for the warm component and $kT_{\text{BB,H}} = 1.11 \pm 0.01$ keV, $R_{\text{BB,H}} = 1.53 \pm 0.03$ km for the hot component, respectively (assuming a distance of 10 kpc; see Section 4), and $\Gamma = 0.9 \pm 0.3$. The observed and unabsorbed

¹⁵ The uncertainty is dominated by the satellite absolute positional accuracy. See <https://cxc.harvard.edu/cal/ASPECT/celmon/>.

¹⁶ Time interval containing 90% of the counts.

Table 1
Observation Log, X-Ray Fluxes, and Limits on Pulsed Radio Emission

| X-Ray Instrument ^a | Obs.ID | Start YYYY Mmm DD hh:mm:ss (TT) | Stop YYYY Mmm DD hh:mm:ss (TT) | Exposure (ks) | Net Count Rate ^b (counts s ⁻¹) | Flux (Obs/Unabs) ^c ($\times 10^{-11}$ erg cm ⁻² s ⁻¹) |
|-------------------------------|-------------|------------------------------------|-----------------------------------|-------------------|----------------------------------------------------------|---------------------------------------------------------------------------------------------|
| ROSAT/SPSPC | rp500012n00 | 1991 Apr 3 20:34:56 | 1991 Apr 3 23:04:12 | 4.5 | <0.008 | <0.008/<0.15 |
| Swift/XRT (PC) | 00999571000 | 2020 Oct 10 14:51:07 | 2020 Oct 10 16:30:29 | 1.7 | 0.47 \pm 0.02 ^d | (4.0 \pm 0.2)/(5.0 \pm 0.2) |
| Swift/XRT (PC) | 00999571001 | 2020 Oct 10 17:53:14 | 2020 Oct 10 22:43:35 | 4.5 | 0.46 \pm 0.01 | (3.8 \pm 0.1)/(4.6 \pm 0.1) |
| XMM-Newton/EPIC-pn (SW) | 0872390501 | 2020 Oct 11 21:07:13 | 2020 Oct 12 03:41:12 | 16.5 ^e | 7.09 \pm 0.02 | (3.96 \pm 0.02)/(5.11 \pm 0.02) |
| NuSTAR/FPMA | 90601331002 | 2020 Oct 12 07:46:09 | 2020 Oct 12 23:26:09 | 29.6 | 0.709 \pm 0.005 | (3.96 \pm 0.02)/(5.11 \pm 0.02) |
| NuSTAR/FPMB | 90601331002 | 2020 Oct 12 07:46:09 | 2020 Oct 12 23:26:09 | 29.4 | 0.666 \pm 0.005 | (3.96 \pm 0.02)/(5.11 \pm 0.02) |
| Swift/XRT (WT) | 00999571002 | 2020 Oct 15 01:15:03 | 2020 Oct 15 20:35:55 | 2.3 | 0.69 \pm 0.02 | (4.1 \pm 0.2)/(5.1 \pm 0.2) |
| Swift/XRT (WT) | 00999571003 | 2020 Oct 16 10:35:46 | 2020 Oct 17 19:04:56 | 2.6 | 0.69 \pm 0.02 | (3.7 \pm 0.2)/(4.6 \pm 0.2) |
| Swift/XRT (WT) | 00999571004 | 2020 Oct 19 04:18:46 | 2020 Oct 19 22:03:56 | 3.3 | 0.66 \pm 0.02 | (3.5 \pm 0.1)/(4.4 \pm 0.1) |
| Swift/XRT (WT) | 00999571005 | 2020 Oct 23 11:33:32 | 2020 Oct 23 14:51:44 | 0.9 | 0.55 \pm 0.03 | (3.3 \pm 0.5)/(4.2 \pm 0.5) |
| Swift/XRT (WT) | 00013840001 | 2020 Oct 29 04:35:55 | 2020 Oct 29 22:34:56 | 2.9 | 0.51 \pm 0.02 | (2.9 \pm 0.1)/(3.6 \pm 0.2) |
| Swift/XRT (WT) | 00013840002 | 2020 Nov 1 15:23:43 | 2020 Nov 2 11:00:56 | 4.1 | 0.42 \pm 0.01 | (3.0 \pm 0.2)/(3.8 \pm 0.2) |
| Swift/XRT (WT) | 00013840003 | 2020 Nov 4 10:24:01 | 2020 Nov 4 23:19:50 | 2.8 | 0.47 \pm 0.01 | (2.5 \pm 0.1)/(3.2 \pm 0.1) |
| Swift/XRT (PC) | 01004219000 | 2020 Nov 5 02:24:07 | 2020 Nov 5 02:52:52 | 1.7 | 0.34 \pm 0.01 | (2.6 \pm 0.3)/(3.1 \pm 0.3) |
| Swift/XRT (WT) | 00013840004 | 2020 Nov 6 11:42:27 | 2020 Nov 6 18:19:56 | 3.8 | 0.48 \pm 0.01 | (2.6 \pm 0.1)/(3.3 \pm 0.1) |
| Swift/XRT (WT) | 00013840005 | 2020 Nov 10 05:01:02 | 2020 Nov 10 10:07:56 | 3.9 | 0.44 \pm 0.01 | (2.3 \pm 0.1)/(2.9 \pm 0.1) |
| Swift/XRT (PC) | 01005428000 | 2020 Nov 11 09:46:28 | 2020 Nov 11 10:15:10 | 1.7 | 0.37 \pm 0.01 | (3.1 \pm 0.5)/(3.6 \pm 0.5) |
| Swift/XRT (WT) | 00013840006 | 2020 Nov 13 01:34:21 | 2020 Nov 13 13:09:56 | 3.6 | 0.33 \pm 0.01 | (2.0 \pm 0.1)/(2.6 \pm 0.1) |

| Radio Instrument | Frequency (GHz) | Bandwidth (MHz) | Start YYYY Mmm DD hh:mm:ss (TT) | Exposure (hr) | Pulsed Flux Density ^f (μ Jy) |
|------------------|--------------------|--------------------|------------------------------------|------------------|-------------------------------------------------|
| SRT | 1.5 | 500 | 2020 Oct 11 16:20:19 | 2.7 | <90 |
| Parkes | 0.96 | 512 | 2020 Oct 12 08:05:33 | 2.9 | <77 |
| Parkes | 1.6 | 768 | 2020 Oct 12 08:05:33 | 2.9 | <39 |
| Parkes | 2.4 | 768 | 2020 Oct 12 08:05:33 | 2.9 | <34 |
| Parkes | 3.4 | 1280 | 2020 Oct 12 08:05:33 | 2.9 | <25 |
| SRT | 6.8 | 900 | 2020 Oct 21 11:59:29 | 2.0 | <45 |
| SRT | 6.8 | 900 | 2020 Oct 21 14:05:39 | 0.7 | <77 |
| SRT | 6.8 | 900 | 2020 Oct 21 15:05:09 | 4.9 | <29 |
| SRT | 6.8 | 900 | 2020 Oct 30 11:02:30 | 7.8 | <23 |
| SRT | 6.8 | 900 | 2020 Nov 6 10:30:00 | 7.1 | <24 |

Notes.

^a The instrumental setup is indicated in brackets: PC = photon counting, SW = small window, WT = windowed timing.

^b The count rate is in the 0.3–10 keV energy range, except for ROSAT (0.1–2.4 keV) and NuSTAR (3–25 keV). The upper limit is quoted at 3σ c.l.

^c The flux is in the 0.3–10 keV energy range. The upper limits are quoted at 3σ c.l., and are computed assuming an absorbed blackbody spectrum with $N_{\text{H}} = 1.07 \times 10^{22}$ cm⁻² and $kT_{\text{BB}} = 0.15$ keV.

^d Corrected for pile-up.

^e Corrected for dead-time.

^f Upper limits are computed using the radiometer equation (Lorimer & Kramer 2004), assuming a pulse duty cycle of 10%.

3

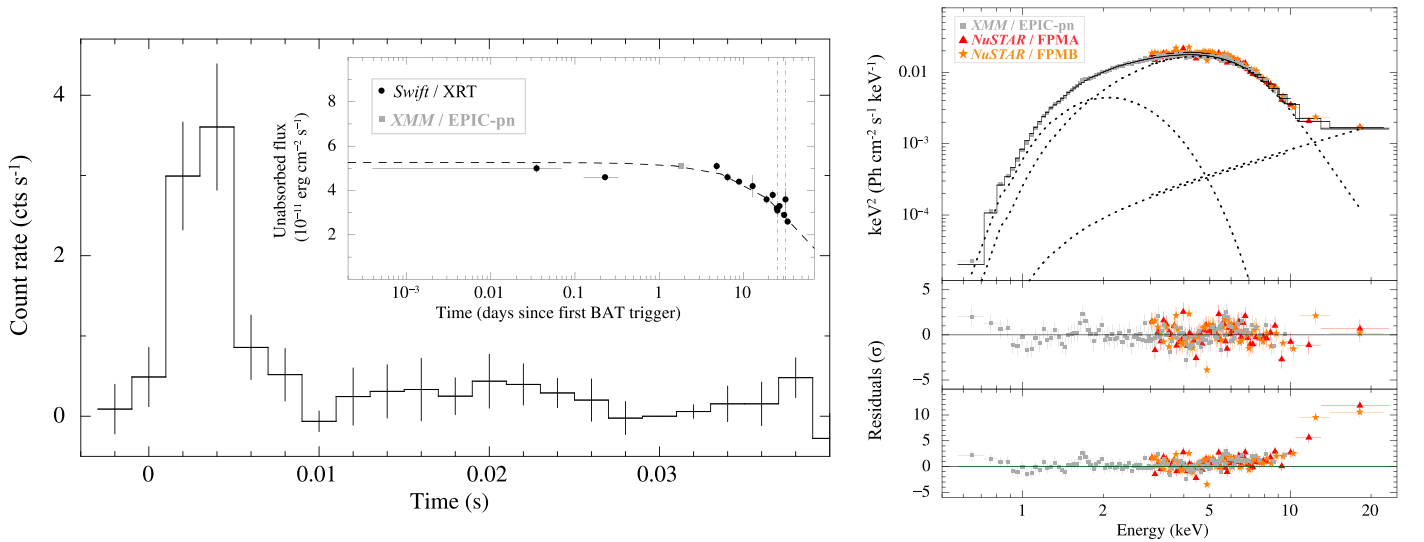


Figure 1. Left: Swift/BAT light curve of the burst that led to the discovery of SGR J1830–0645 (15–50 keV energy range; time bin: 2 ms; the start time is arbitrary). The inset shows the evolution of the 0.3–10 keV unabsorbed flux of SGR J1830–0645 measured over a baseline of about one month since the burst trigger (MJD 59132.6176). The dashed line marks the best-fitting exponential function. The vertical dotted–dashed lines mark the epochs of the other two bursts detected by the BAT (MJD 59158.0986 and 59164.4071; Gropp et al. 2020a, 2020b). Right, top: unfolded spectrum extracted from the XMM-Newton/EPIC-pn (gray), NuSTAR/FPMA (red), and NuSTAR/FPMB (orange) data. The solid line indicates the best-fitting model, the dotted lines show the contribution of the different spectral components. Middle: post-fit residuals. Bottom: residuals obtained after removing the power-law component from the model.

fluxes were $(4.33 \pm 0.03) \times 10^{-11}$ and $(5.54 \pm 0.03) \times 10^{-11}$ erg cm $^{-2}$ s $^{-1}$ in the 0.3–25 keV energy range, with a fractional contribution of the power-law component of $\simeq 6\%$ in the same band.

Then, we fit an absorbed double-blackbody model to all Swift/XRT data, fixing the column density at $N_{\text{H}} = 1.07 \times 10^{22}$ cm $^{-2}$, and allowing all other parameters to vary across the data sets. The observed and unabsorbed fluxes derived from the above model are reported in Table 1, while the evolution of the unabsorbed flux is shown in the inset of the left panel in Figure 1. The unabsorbed flux decreased by a factor of ~ 2 along our campaign, from $\sim 5 \times 10^{-11}$ erg cm $^{-2}$ s $^{-1}$ at peak to $\sim 2.5 \times 10^{-11}$ erg cm $^{-2}$ s $^{-1}$ about one month later (0.3–10 keV). Its time evolution can be adequately described so far by an exponential function with e -folding time $\tau = 55 \pm 2$ days ($\chi_r^2 = 1.42$ for 13 d.o.f.; Figure 1).

SGR J1830–0645 was in the field of view of ROSAT/PSPC in a pointing performed on 1991 April 3 (see Table 1). The source is not detected, and we set an upper limit on the net count rate of 0.008 counts s $^{-1}$ (3σ c.l.; 0.1–2.4 keV). Assuming emission from the entire surface ($R_{\text{NS}} = 10$ –15 km) and a source distance of 10 kpc, we estimate that the blackbody temperature should be $\lesssim 0.15$ keV to be consistent with the above limit. The corresponding limits on the observed and unabsorbed flux are $F_{\text{X,obs}} < 8 \times 10^{-14}$ erg cm $^{-2}$ s $^{-1}$ and $F_{\text{X,unabs}} < 1.5 \times 10^{-12}$ erg cm $^{-2}$ s $^{-1}$ (0.3–10 keV).

2.2.3. Timing Analysis and Phase-resolved Spectroscopy

The EPIC-pn, Swift/XRT, and NuSTAR source event files were used to study the magnetar timing properties. We built up a phase-coherent timing solution starting from the period $P = 10.41572(1)$ s inferred from the EPIC-pn data sets (those with the largest statistics), and employing a phase-fitting technique. Within a baseline of about 34 days (2020 October 10–November 13), we clearly detected a first period derivative component in the signal phase history, and derived the following timing solution:

$P = 10.415724(1)$ s, $\dot{P} = 7(1) \times 10^{-12}$ s s $^{-1}$ at the reference epoch $T_0 = 59133.0$ MJD. The \dot{P} value is in agreement with that derived by Ray et al. (2020) using NICER data sets. Our timing solution implies an rms variability of ~ 145 ms, corresponding to a timing noise level $< 2\%$, similar to the range of values observed in other isolated NSs. We set a 3σ upper limit on the second period derivative of $|\ddot{P}| < 2 \times 10^{-17}$ s s $^{-2}$.

Figure 2 shows the background-subtracted light curves extracted from the EPIC-pn and NuSTAR data sets over different energy intervals, folded using the above ephemeris. Pulsed emission was detected up to an energy of ~ 15 keV. The pulse profile displays an apparent complex morphology below 10 keV, with a pronounced dip close to the main peak, a weaker peak in the rising part of the profile, and small-amplitude structures at minimum (seemingly less prominent above ~ 4 keV). The profile appears to evolve to a relatively simpler shape at higher energies in the 12–15 keV energy range. The pulse peak in this range lags the main peak observed at lower energies by 0.11 ± 0.06 spin phase cycles. The background-subtracted peak-to-peak semiamplitude increases from $(63 \pm 2)\%$ below 3 keV to $(71 \pm 3)\%$ in the 4–10 keV band, and drops to $\sim 20\%$ in the 10–12 and 12–15 keV ranges. We set a 3σ upper limit of 20% in the 15–25 keV range (Figure 2). The marked changes in the pulse profile amplitude at energies where the power-law spectral component dominates the source emission (Figure 1) indicate that the power-law tail is also pulsed, though to a smaller extent than the low-energy blackbody components.

We performed a phase-resolved spectral analysis over the 0.3–10 keV energy range using the EPIC-pn data. We extracted spectra from 50 phase intervals of width 0.02 rotational cycles, and fitted them using an absorbed double-blackbody model. In the fits, the column density was held fixed at the phase-averaged value ($N_{\text{H}} = 1.07 \times 10^{22}$ cm $^{-2}$; Section 2.2.2), while all other parameters were allowed to vary. Figure 2 shows the evolution of the spectral parameters and unabsorbed fluxes of both thermal components, as well as their flux ratio, along the

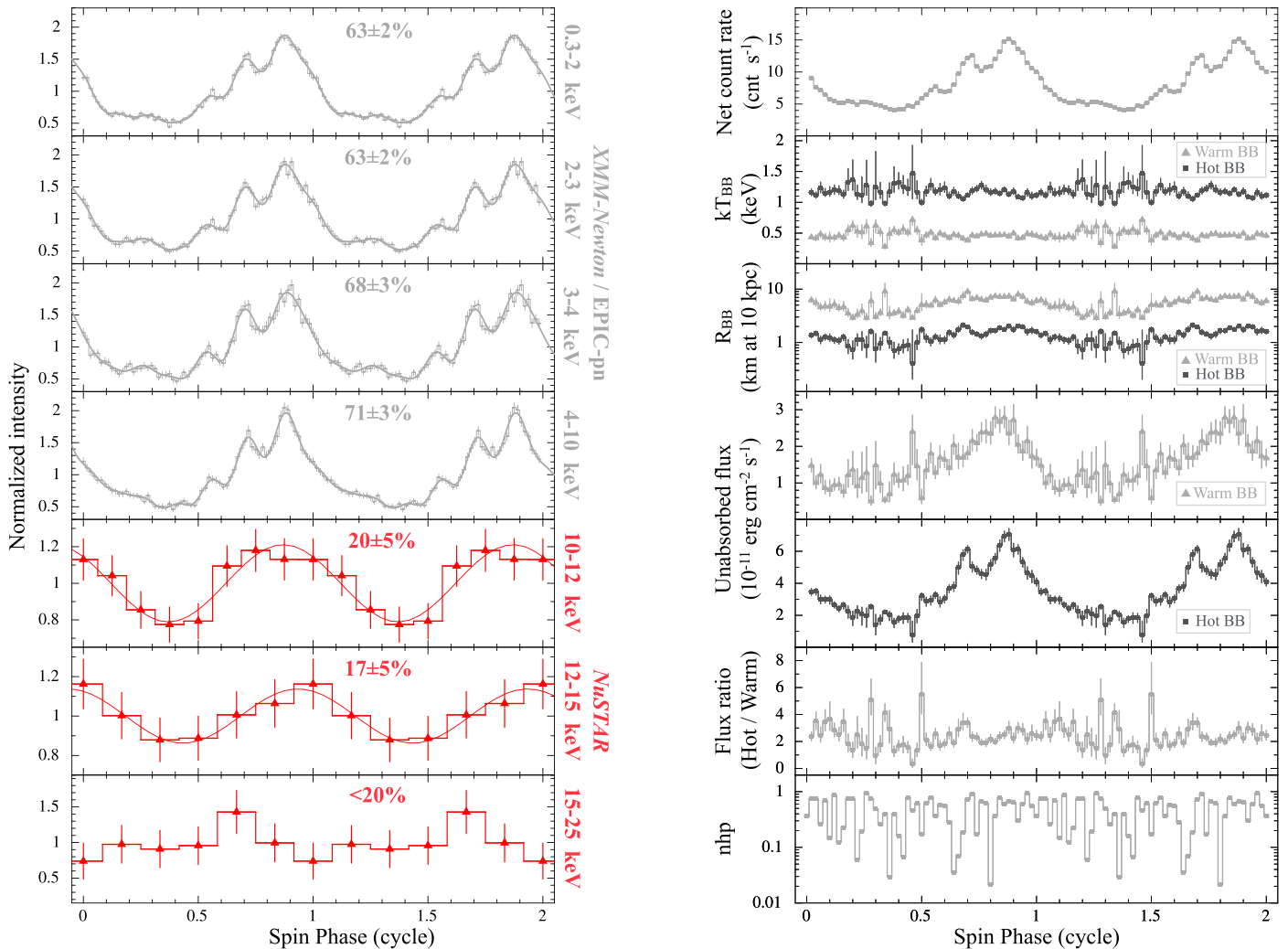


Figure 2. Left: energy-resolved background-subtracted pulse profiles of SGR J1830–0645 extracted from XMM-Newton/EPIC-pn (gray) and NuSTAR (red) data. The best-fitting models obtained by using seven sinusoidal components (fundamental plus harmonics) for EPIC-pn and a single sinusoidal component (fundamental) for NuSTAR are indicated with solid lines. The corresponding pulsed fraction values (or the 3σ upper limit for the 15–25 keV range) are reported in each panel. Right: results of the spin phase-resolved spectroscopy of EPIC-pn data in the 0.3–10 keV range. From top to bottom: background-subtracted pulse profile; blackbody temperature, radius (assuming a distance of 10 kpc) and 0.3–10 keV unabsorbed flux for the warm (light gray) and hot (dark gray) components; hot-to-warm blackbody unabsorbed flux ratio; nhp values derived from the χ^2 and the d.o.f. of the fit of each spectrum. All uncertainties are at 1σ c.l.

rotational phase. The complex spin modulation pattern for the soft X-ray emission can be ascribed to changes in the blackbody radius of both components. The smaller, hotter region traces more closely the fine structures seen in the pulse profile (e.g., the dip close to the peak; Figure 2). On the other hand, the scarce counting statistics available in the energy range 12–15 keV (less than 500 net counts summing up the NuSTAR FPMs) precludes an assessment of possible variability of the power-law slope along the rotational phase.

2.2.4. Search for Short X-Ray Bursts

Short X-ray bursts were searched for by applying the procedure described by Gavril et al. (2004) and Scholz & Kaspi (2011; see also Borghese et al. 2020). We extracted light curves with different time resolutions (2^{-4} , 2^{-5} , 2^{-6} s) to improve sensitivity to bursts of different durations, except for Swift/XRT PC-mode light curves that were binned at the timing resolution (2.5073 s). For each observation, we

calculated the Poisson probability of an event to be a random fluctuation with respect to the average number of counts per bin. Any bin with a probability smaller than $10^{-4}(NN_{\text{trials}})^{-1}$, where N is the total number of time bins and N_{trials} is the number of timing resolutions used in the search, was flagged as part of a burst. We detected 12 bursts in the Swift/XRT light curves (Figure 3 and Table 2). No bursts were found in the XMM-Newton and NuSTAR data sets.

3. Radio Searches

Table 1 reports a log of the radio observations, performed using the Sardinia Radio Telescope (SRT; Bolli et al. 2015; Prandoni et al. 2017) and Parkes.

3.1. Sardinia Radio Telescope Observations

The SRT observed SGR J1830–0645 at 1.5 GHz (L band) on October 11 for 2.7 hr and at 6.8 GHz (C band) on October 21, 30 and November 6, for a total exposure of 22.5 hr. Data

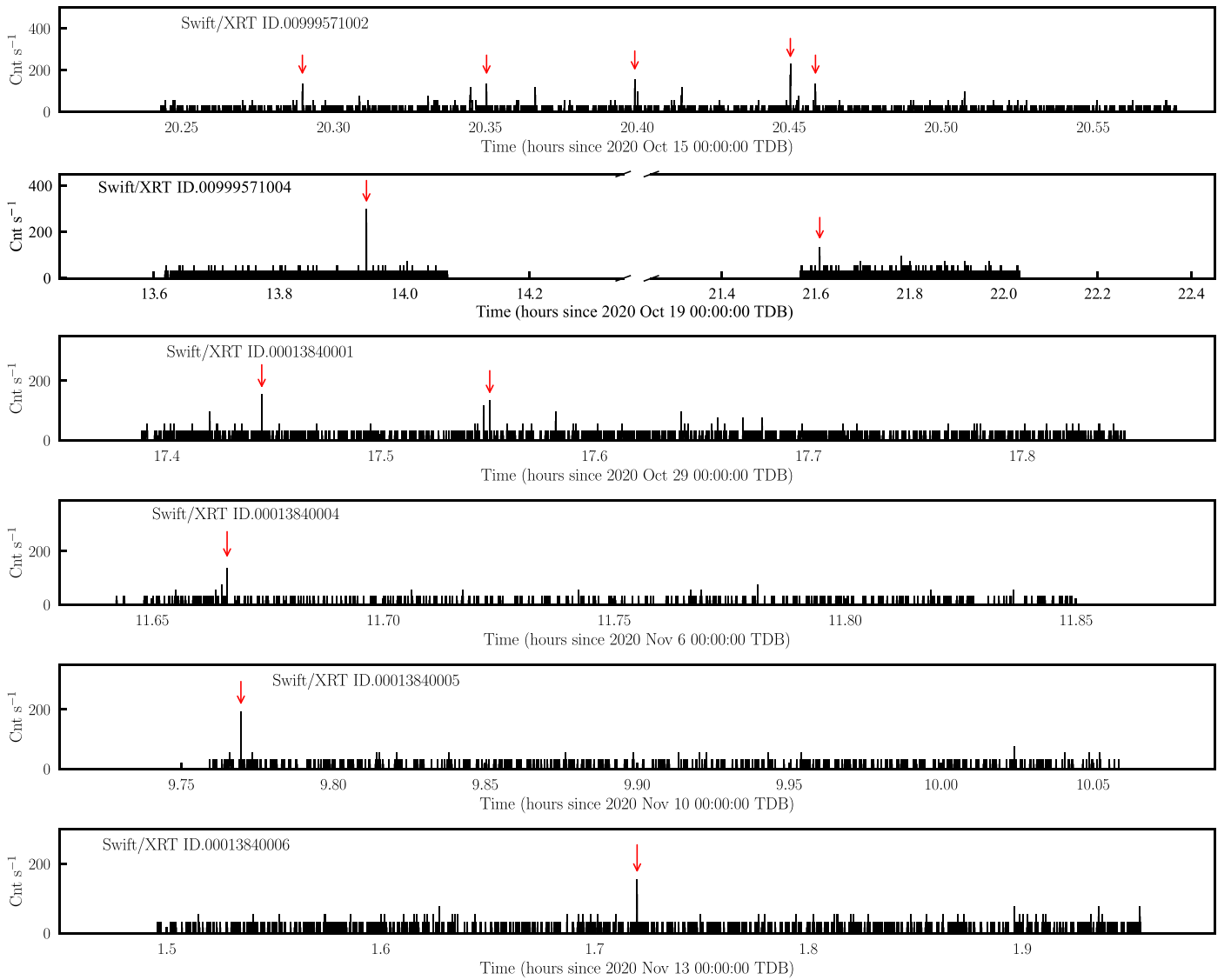


Figure 3. Light curves of SGR J1830–0645 extracted from the Swift/XRT data in which we detected bursts (0.3–10 keV; time bin: 62.5 ms). All events fulfilling our detection criterion are marked by arrows.

were recorded with the ATNF PDFB backend in search mode over a bandwidth of 500 MHz in *L* band and 900 MHz in *C* band, with a spectral resolution of 1 MHz. Total intensity data were 2 bit sampled every 0.1 ms for the *L* band and 0.125 ms for the *C* band.

All data were folded using the X-ray ephemeris and searched over a dispersion measure (DM) range of 0–1200 pc cm⁻³ and a spin period range of ± 1 ms around the nominal value (after removing the most prominent radio frequency interference; RFI), using the software packages DSPSR (van Straten & Bailes 2011) and PSRCHIVE (Hotan et al. 2004). No pulsations were detected down to a folded signal-to-noise ratio of $S/N = 10$. The corresponding flux density upper limits are reported in Table 1.

A search for bursts was performed on all data using the SPANDAK pipeline (Gajjar et al. 2018), sampling a DM range of 0–1200 pc cm⁻³. After dedispersion, the time series were searched for pulses using matched-filtering with a maximum window size of 32 ms. After a first automatic sifting of the generated candidates, visual inspection was performed on the events that passed the selection. No bursts were found at either *L* or *C* band.

3.2. Parkes Observations

The Parkes radio telescope observed SGR J1830–0645 on October 12, starting at 08:04:24 UT for 2.9 hr, simultaneously with NuSTAR. Data were recorded with the ultra-wide-bandwidth low-frequency receiver (UWL; Hobbs et al. 2020) over a bandwidth of 3328 MHz centered at 2368 MHz. Full Stokes data were 4 bit sampled every 0.128 ms. Four separate data sets covering different subbands were created with different spectral resolutions so as to achieve a maximum broadening of a few ms for a signal with $DM = 600$ pc cm⁻³¹⁷ (band b0, from 704 to 1216 MHz, split into 2048 frequency channels; b1, 1216–1984 MHz, 768 channels; b2, 1984–2752 MHz, 384 channels; b3, 2752–4032 MHz, 320 channels).

To search for persistent pulsations, the data of the subbands were folded using the X-ray ephemeris. After RFI removal, the frequency resolution of the folded data was scaled uniformly down to 4 MHz, and data were summed together. A search over

¹⁷ This is the maximum value expected for our Galaxy in the direction of SGR J1830–0645, according to the NE2001 electron density model (Cordes & Lazio 2002).

Table 2
Log of X-Ray Bursts Detected in the Swift/XRT Data Sets

| Obs.ID ^a | Burst Epoch YYYY Mmm DD hh:mm: ss (TDB) | Duration ^b (ms) | Fluence ^c (net counts) |
|---------------------|-----------------------------------------------|-------------------------------|--------------------------------------|
| 00999571002 #1 | 2020 Oct 15 20:17:23 | 62.5 | 6 |
| #2 | 20:21:01 | 62.5 | 6 |
| #3 | 20:23:57 | 62.5 | 7 |
| #4 | 20:27:01 | 62.5 | 11 |
| #5 | 20:27:31 | 62.5 | 6 |
| 00999571004 #1 | 2020 Oct 19 13:56:24 | 62.5 | 15 |
| #2 | 21:36:31 | 62.5 | 6 |
| 00013840001 #1 | 2020 Oct 29 17:26:40 | 62.5 | 7 |
| #2 | 17:33:03 | 62.5 | 6 |
| 00013840004 #1 | 2020 Nov 6 11:39:58 | 62.5 | 6 |
| 00013840005 #1 | 2020 Nov 10 09:46:10 | 62.5 | 9 |
| 00013840006 #1 | 2020 Nov 13 01:43:12 | 62.5 | 7 |

Notes.

^a The notation #N corresponds to the burst number in a given observation.

^b The duration shall be considered as an approximate value. It was estimated as the coarser time resolution at which the burst is detected, or as the sum of the time bins showing enhanced emission for the case of the burst 00999571004 #1.

^c The fluence refers to the 0.3–10 keV energy range.

a DM range of 0–1200 pc cm⁻³ spanning ±1 ms around the nominal spin period was performed on the entire observing bandwidth. No pulsations were detected down to a folded S/N = 10. The flux density upper limits in the different subbands are reported in Table 1.

The single-pulse analysis was performed using the procedure described in Section 3.1 and the same parameters. The subbanding did not affect the search since we are looking for impulsive bursts. After the RFI removal, the data were dedispersed from 0 to 1200 pc cm⁻³. No bursts were found at any band.

4. Discussion

In 2020 October, SGR J1830–0645 entered its first detected outburst phase, revealing to be a new Galactic magnetar. The source emitted numerous X-ray bursts since the beginning of the outburst and during our monitoring campaign (Sections 2.2.1 and 2.2.4; see also Palmer 2020; Ray et al. 2020). This is a distinctive phenomenology usually observed in magnetars during an active phase. Our campaign allowed us to measure the spin period ($P = 10.415724(1)$ s) and its first derivative ($\dot{P} = 7(1) \times 10^{-12}$ s s⁻¹) at the outburst peak (Section 2.2.3), hence to estimate a surface dipolar magnetic field $B_{\text{dip}} \sim 6.4 \times 10^{19} (P\dot{P})^{1/2} \approx 5.5 \times 10^{14}$ G at pole (using the vacuum dipole formula), a spin-down luminosity $\dot{E}_{\text{rot}} = 4\pi^2 I \dot{P} P^{-3} \approx 2.4 \times 10^{32}$ erg s⁻¹ (where $I \approx 10^{45}$ g cm² is the moment of inertia of the NS) and a characteristic age $\tau_c = P/2\dot{P} \approx 24$ kyr.

The extension of the Galaxy in the direction of SGR J1830–0645 estimated from the maps of Hou & Han (2014) and the similarity between the column density derived from our spectral fits ($N_{\text{H}} \sim 1.07 \times 10^{22}$ cm⁻²) and that expected in the direction of the source within the Galaxy ($N_{\text{H,Gal}} \sim 1.1 \times 10^{22}$ cm⁻²; Willingale et al. 2013) suggest a distance $D \gtrsim 5$ kpc. In the following, we rescale all quantities to a distance of $D = 10$ kpc. Assuming isotropic emission, the X-ray luminosity at the outburst peak is then $L_{\text{X,p}} \sim 6 \times 10^{35} d_{10}^2$ erg s⁻¹, while the limit we

derived for the quiescent X-ray luminosity is $L_{\text{X,q}} < 2 \times 10^{34} d_{10}^2$ erg s⁻¹ (0.3–10 keV; $d_{10} = D/10$ kpc; see Section 2.2.2).

We studied the evolutionary history of SGR J1830–0645 using a two-dimensional magneto-thermal evolutionary model (Viganò et al. 2012, 2013, 2020). We used crustal-confined models consisting of an initial poloidal dipolar field ($B_{\text{dip,in}}$) plus a toroidal field ($B_{\text{tor,in}}$), and assumed for simplicity an equal amount of magnetic energy in the two components. We find that the evolution of an initial configuration with $B_{\text{dip,in}} \sim 10^{15}$ G and $B_{\text{tor,in}} \sim 10^{16}$ G provides a close match to the current P and \dot{P} after ~ 23 kyr. We thus obtain an age $\tau_{\text{th}} \sim 23$ kyr for SGR J1830–0645, similar to its characteristic age, and predict a quiescent bolometric thermal luminosity at τ_{th} that would be just below our current upper limit on $L_{\text{X,q}}$. The good agreement between τ_{th} and τ_c is due to the fact that the dissipation of the magnetic field is not yet substantial at this evolutionary stage. At later stages, τ_c will overestimate the real age because the electromagnetic torque decreases in time due to magnetic field dissipation, while τ_{th} usually remains consistent with the real age.

From its properties and simulated history, we find that SGR J1830–0645 is a middle age magnetar that had relatively strong magnetic energy at birth. The gray shaded region in Figure 4 shows the evolution of the spin period and luminosity of SGR J1830–0645 (taking into account uncertainties due to the assumption of light or heavy elements in the envelope), compared with current values for other magnetars. This region encompasses also two other magnetars with rather different magnetic field strengths, CXOU J171405.7–381031 and XTE J1810–197 (see the color scale in the figure). The properties of SGR J1830–0645 at birth were probably similar to those of CXOU J171405.7–381031, but different from those of XTE J1810–197. Indeed, CXOU J171405.7–381031 has a stronger magnetic field and a younger age than SGR J1830–0645, and it might be now at an earlier stage of a similar evolutionary scenario. On the other hand, XTE J1810–197 is characterized by a luminosity and spin period that might be potentially compatible with those expected if this source were at an earlier stage of the same evolutionary path of SGR J1830–0645, but its magnetic field is already smaller than that of SGR J1830–0645.

The X-ray emission properties observed from SGR J1830–0645 soon after the outburst onset are in line with those of other magnetars (Coti Zelati et al. 2018 and references therein), and fit well within the resonant Compton scattering scenario (RCS; Thompson et al. 2002; Rea et al. 2008; Wadiasingh et al. 2018; see also Turolla et al. 2015 and references therein). The dominance of the thermal over the nonthermal (power-law) component (Section 2.2.2) suggests that the magnetospheric twist is restricted to a bundle of current-carrying field lines. Ohmic dissipation of the returning currents on the star surface leads to the appearance of localized hot spots (Beloborodov 2009). Heated regions may form on the surface also as a consequence of heat released deeper in the crust by local dissipation of magnetic energy (Pons & Rea 2012). In this respect, our analysis suggests the existence of two heated regions of different temperatures and sizes on the surface of SGR J1830–0645: an extended warm region (average blackbody temperature ~ 0.45 keV and radius ~ 6 km), and a small hot region (temperature ~ 1.1 keV and radius ~ 1.5 km). According to our analysis, the modulation of the light curve is (almost) entirely due to the change of the visible area of these regions, the temperatures being fairly constant along the spin phase (Figure 2). The phase-alignment between the light-curve

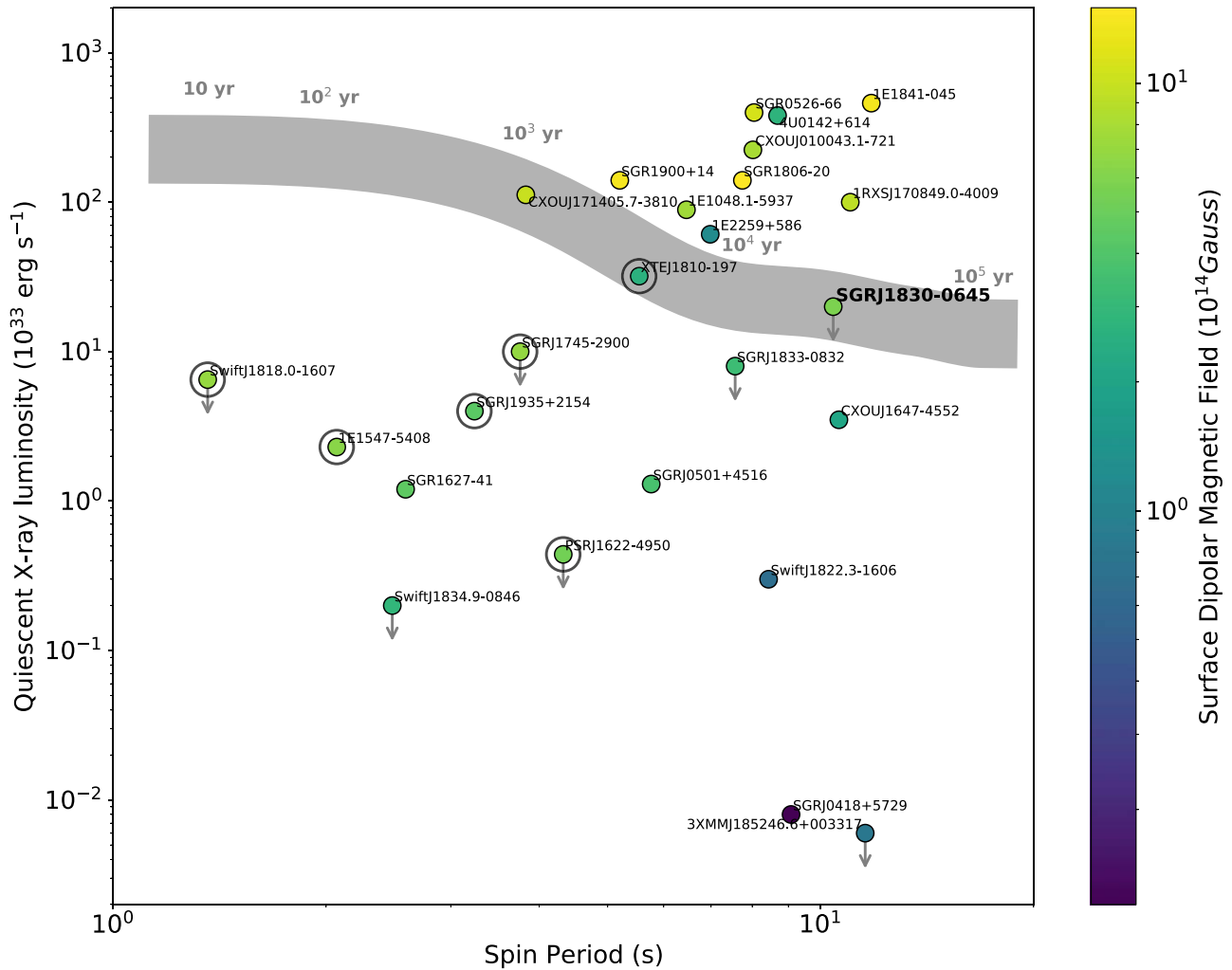


Figure 4. Quiescent X-ray luminosity as a function of the spin period for magnetars, including SGR J1830–0645 (in bold). Circles mark radio-loud magnetars. The gray shaded region shows the magneto-thermal evolutionary path of SGR J1830–0645 according to the model discussed in the text. Values are taken from The Magnetar Outburst Online Catalog (<http://magnetars.ice.csic.es>).

profiles associated with the two blackbody components is indicative of a scenario in which the hot and the warm regions are not spatially separated. A more plausible picture is that what we actually see is a single heated spot with a complex shape where an extended warm region is surrounded by a smaller hotter region with an asymmetric structure (the former producing the relatively broad peak observed in the light-curve profile, the latter resulting in the two prominent narrow peaks separated by ~ 0.2 rotational phase cycles; see Figure 2). Indeed, recent 3D simulations have shown that heat injected in a localized region of the crust of a magnetar flows anisotropically to the surface, leading to the appearance of a hot spot with a complex shape and a nonuniform temperature distribution (De Grandis et al. 2020). Soft, thermal photons coming from such a spot can produce a complex pulse profile with a high pulsed fraction, which would be smaller ($\lesssim 20\%$) in the case of two circular, antipodal hot spots (Albano et al. 2010; Turolla & Nobili 2013). The pulsed fraction decrease going from lower to higher energies (up to ~ 25 keV) is different from what is observed in other magnetars (see, e.g., An et al. 2015, and references therein). Different trends of the pulsed fraction variability with energy can be envisaged within the RCS scenario, depending on the viewing angles as well as the location and velocity distribution of the charged particles in

the magnetosphere that up-scatter thermal photons. In the case of SGR J1830–0645, the RCS mechanism tends to wash out the imprint of the (pulsed) primary emission.

Our nondetection of radio pulsations from SGR J1830–0645 is not that surprising per se. Similarly to canonical radio pulsars, radio-loud magnetars are generally characterized by high spin-down luminosities $\dot{E}_{\text{rot}} \gtrsim 10^{33}$ erg s $^{-1}$, implying $L_{X,q}/\dot{E}_{\text{rot}} < 1$ (Rea et al. 2012; the only outlier being XTE J1810–197). A reliable estimate of $L_{X,q}/\dot{E}_{\text{rot}}$ for SGR J1830–0645 is difficult owing to uncertainties on the distance and the nondetection of the source in pre-outburst X-ray data. However, if its quiescent luminosity is not much below our quoted limit, it would have $L_{X,q}/\dot{E}_{\text{rot}} \gg 1$, in line with being radio-silent. Alternatively, SGR J1830–0645 might be radio-loud but undetectable due to unfavorable beaming.

Future high-sensitive X-ray observations will be key in mapping the evolution of the heated spot on the star surface and the long-term contribution of magnetospheric currents to the broadband X-ray emission of SGR J1830–0645.

















We thank N. Schartel and F. Harrison for approving Target of Opportunity observations with XMM-Newton and NuSTAR in the Director’s Discretionary Time, and the XMM-Newton and NuSTAR SOCs for carrying out the observations. We also

thank B. Cenko and the Swift duty scientists and science planners for making the Swift Target of Opportunity observations possible. This research is based on observations with XMM-Newton (ESA/NASA), NuSTAR (CalTech/NASA/JPL), and Swift (NASA/ASI/UKSA) and on data retrieved through the NASA/GSFC's HEASARC archives. The Sardinia Radio Telescope is funded by the Italian MIUR, ASI, and the Autonomous Region of Sardinia, and is operated as a National Facility by INAF. We used data collected at the Parkes radio telescope (proposal No. P1083), part of the Australia Telescope National Facility which is funded by the Australian Government for operation as a National Facility managed by CSIRO. We acknowledge the Wiradjuri people as the traditional owners of the Observatory site. F.C.Z. and A.B. are supported by Juan de la Cierva fellowships. F.C.Z., A.B., N.R., C.D., and D.V. are supported by the ERC Consolidator Grant "MAGNESIA" (No. 817661) and acknowledge funding from grants SGR2017-1383 and PGC2018-095512-BI00. G.L.I., P.E., R.T., and A.T. acknowledge financial support from the Italian MIUR through PRIN grant 2017LJ39LM. G.L.I. also acknowledges funding from ASI-INAF agreements I/037/12/0 and 2017-14-H.O. M.B., A.P., and A.R. acknowledge financial support from the research grant "iPeska" (PI: A. Possenti) funded under the INAF national call PRIN-SKA/CTA with Presidential Decree 70/2016. A.R. acknowledges continuing valuable support from the Max-Planck Society. We acknowledge the support of the PHAROS COST Action (CA16214).

Facility: XMM-Newton (EPIC), Swift (BAT, XRT), NuSTAR, ROSAT (PSPC), Parkes, SRT, ADS, HEASARC.

Software: HEASOFT (v.6.28; Nasa High Energy Astrophysics Science Archive Research Center (Heasarc), 2014), NUSKYBGD (Wik et al. 2014), SAOImageDS9 (v.8.1; Joye & Mandel 2003), SAS (v.19; Gabriel et al. 2004), XSPEC (v.12.11.1; Arnaud 1996), DSPSR (van Straten & Bailes 2011), PSRCHIVE (Hotan et al. 2004), SPANDAK (<https://github.com/gajjarv/PulsarSearch>), Astropy (v.4.2; Astropy Collaboration et al. 2013, 2018), MATPLOTLIB (v3.3.3; Hunter 2007), NUMPY (v1.19.4; Harris et al. 2020).

ORCID iDs

F. Coti Zelati  <https://orcid.org/0000-0001-7611-1581>
 A. Borghese  <https://orcid.org/0000-0001-8785-5922>
 G. L. Israel  <https://orcid.org/0000-0001-5480-6438>
 N. Rea  <https://orcid.org/0000-0003-2177-6388>
 P. Esposito  <https://orcid.org/0000-0003-4849-5092>
 M. Pilia  <https://orcid.org/0000-0001-7397-8091>
 M. Burgay  <https://orcid.org/0000-0002-8265-4344>
 A. Possenti  <https://orcid.org/0000-0001-5902-3731>
 A. Corongiu  <https://orcid.org/0000-0002-5924-3141>
 A. Ridolfi  <https://orcid.org/0000-0001-6762-2638>
 C. Dehman  <https://orcid.org/0000-0003-0554-7286>
 D. Viganò  <https://orcid.org/0000-0001-7795-6850>
 R. Turolla  <https://orcid.org/0000-0003-3977-8760>
 S. Zane  <https://orcid.org/0000-0001-5326-880X>
 A. Tiengo  <https://orcid.org/0000-0002-6038-1090>
 E. F. Keane  <https://orcid.org/0000-0002-4553-655X>

References

Albano, A., Turolla, R., Israel, G. L., et al. 2010, *ApJ*, 722, 788
 An, H., Archibald, R. F., Hascoët, R., et al. 2015, *ApJ*, 807, 93

Arnaud, K. A. 1996, in ASP Conf. Ser. 101, *Astronomical Data Analysis Software and Systems V*, XSPEC: The First Ten Years, ed. G. H. Jacoby & J. Barnes (San Francisco, CA: ASP), 17
 Astropy Collaboration, Price-Whelan, A. M., Sipőcz, B. M., et al. 2018, *AJ*, 156, 123
 Astropy Collaboration, Robitaille, T. P., Tollerud, E. J., et al. 2013, *A&A*, 558, A33
 Beloborodov, A. M. 2009, *ApJ*, 703, 1044
 Bolli, P., Orlati, A., Stringhetti, L., et al. 2015, *JAI*, 4, 1550008
 Borghese, A., Coti Zelati, F., Rea, N., et al. 2020, *ApJL*, 902, L2
 Burrows, D. N., Hill, J. E., Nousek, J. A., et al. 2005, *SSRv*, 120, 165
 Collazzi, A. C., Kouveliotou, C., van der Horst, A. J., et al. 2015, *ApJS*, 218, 11
 Cordes, J. M., & Lazio, T. J. W. 2002, arXiv:astro-ph/0207156
 Coti Zelati, F., Borghese, A., Rea, N., et al. 2020, *A&A*, 633, A31
 Coti Zelati, F., Rea, N., Pons, J. A., et al. 2018, *MNRAS*, 474, 961
 De Grandis, D., Turolla, R., Wood, T. S., et al. 2020, *ApJ*, 903, 40
 Duncan, R. C., & Thompson, C. 1992, *ApJL*, 392, L9
 Esposito, P., Rea, N., & Israel, G. L. 2021, in *Magnetars: A Short Review and Some Sparse Considerations*, ed. T. M. Belloni, M. Méndez, & C. Zhang (Berlin: Springer), 97
 Gabriel, C., Denby, M., Fyfe, D. J., et al. 2004, in ASP Conf. Ser. 314, *Astronomical Data Analysis Software and Systems (ADASS) XIII, The XMM-Newton SAS—Distributed Development and Maintenance of a Large Science Analysis System: A Critical Analysis*, ed. F. Ochsenbein, M. G. Allen, & D. Egret (San Francisco, CA: ASP), 759
 Gajjar, V., Siemion, A. P. V., Price, D. C., et al. 2018, *ApJ*, 863, 2
 Gavriil, F. P., Kaspi, V. M., & Woods, P. M. 2004, *ApJ*, 607, 959
 Gogus, E., Kouveliotou, C., & Younes, G. 2020a, *ATel*, 14085, 1
 Gogus, E., Kouveliotou, C., & Younes, G. 2020b, *ATel*, 14097, 1
 Gropp, J. D., Kennea, J. A., Klingler, N. J., et al. 2020a, *GCN*, 28838, 1
 Gropp, J. D., Klingler, N. J., Kuin, N. P. M., et al. 2020b, *GCN*, 28879, 1
 Harris, C. R., Millman, K. J., van der Walt, S. J., et al. 2020, *Natur*, 585, 357
 Harrison, F. A., Craig, W. W., Christensen, F. E., et al. 2013, *ApJ*, 770, 103
 Hobbs, G., Manchester, R. N., Dunning, A., et al. 2020, *PASA*, 37, e012
 Hotan, A. W., van Straten, W., & Manchester, R. N. 2004, *PASA*, 21, 302
 Hou, L. G., & Han, J. L. 2014, *A&A*, 569, A125
 Hunter, J. D. 2007, *CSE*, 9, 90
 Joye, W. A., & Mandel, E. 2003, in ASP Conf. Ser. 295, *Astronomical Data Analysis Software and Systems XII*, ed. E. Payne, R. I. Jedrzejewski, & R. N. Hook (San Francisco, CA: ASP), 489
 Kaspi, V. M., & Beloborodov, A. M. 2017, *ARA&A*, 55, 261
 Lorimer, D. R., & Kramer, M. 2004, *Handbook of Pulsar Astronomy* (Cambridge: Cambridge Univ. Press)
 Nasa High Energy Astrophysics Science Archive Research Center (Heasarc) 2014, HEASOFT: Unified Release of FTOOLS and XANADU, Astrophysics Source Code Library, ascl:1408.004
 Olausen, S. A., & Kaspi, V. M. 2014, *ApJS*, 212, 6
 Page, K. L., Barthelmy, S. D., Klingler, N. J., et al. 2020, *ATel*, 14083, 1
 Palmer, D. 2020, *ATel*, 14208, 1
 Pons, J. A., & Rea, N. 2012, *ApJL*, 750, L6
 Prandoni, I., Murgia, M., Tarchi, A., et al. 2017, *A&A*, 608, A40
 Ray, P. S., Younes, G., Guver, T., et al. 2020, *ATel*, 14112, 1
 Rea, N., Pons, J. A., Torres, D. F., & Turolla, R. 2012, *ApJL*, 748, L12
 Rea, N., Zane, S., Turolla, R., et al. 2008, *ApJ*, 686, 1245
 Scholz, P., & Kaspi, V. M. 2011, *ApJ*, 739, 94
 Strüder, L., Briel, U., Dennerl, K., et al. 2001, *A&A*, 365, L18
 Thompson, C., Lyutikov, M., & Kulkarni, S. R. 2002, *ApJ*, 574, 332
 Tohuvavohu, A. 2020, *ATel*, 14088, 1
 Turner, M. J. L., Abbey, A., Arnaud, M., et al. 2001, *A&A*, 365, L27
 Turolla, R., & Nobili, L. 2013, *ApJ*, 768, 147
 Turolla, R., Zane, S., & Watts, A. L. 2015, *RPPH*, 78, 116901
 van Straten, W., & Bailes, M. 2011, *PASA*, 28, 1
 Viganò, D., Garcia-Garcia, A., Pons, J. A., et al. 2020, *Comput. Phys. Commun.*, submitted
 Viganò, D., Pons, J. A., & Miralles, J. A. 2012, *CoPhC*, 183, 2042
 Viganò, D., Rea, N., Pons, J. A., et al. 2013, *MNRAS*, 434, 123
 Wadiasingh, Z., Baring, M. G., Gonthier, P. L., & Harding, A. K. 2018, *ApJ*, 854, 98
 Wik, D. R., Hornstrup, A., Molendi, S., et al. 2014, *ApJ*, 792, 48
 Willingale, R., Starling, R. L. C., Beardmore, A. P., et al. 2013, *MNRAS*, 431, 394
 Wilms, J., Allen, A., & McCray, R. 2000, *ApJ*, 542, 914
 Younes, G., Baring, M. G., Kouveliotou, C., et al. 2017, *ApJ*, 851, 17
 Younes, G., Guver, T., Wadiasingh, Z., et al. 2020, *ATel*, 14086, 1